

The CO universe: Modelling CO emission and H₂ abundance in cosmological galaxy formation simulations

Shigeki Inoue^{1,2,3,4*}, Naoki Yoshida^{3,4,5} & Hidenobu Yajima¹

¹Center for Computational Sciences, University of Tsukuba, Ten-nodai, 1-1-1 Tsukuba, Ibaraki 305-8577, Japan

²Chile Observatory, National Astronomical Observatory of Japan, Mitaka, Tokyo 181-8588, Japan

³Kavli Institute for the Physics and Mathematics of the Universe (WPI), UTIAS, The University of Tokyo, Chiba 277-8583, Japan

⁴Department of Physics, School of Science, The University of Tokyo, Bunkyo, Tokyo 113-0033, Japan

⁵Research Center for the Early Universe, School of Science, The University of Tokyo, Bunkyo, Tokyo 113-0033, Japan

Accepted XXX. Received YYY; in original form ZZZ

ABSTRACT

We devise a physical model of formation and distribution of molecular gas clouds in galaxies. We use the model to predict the intensities of rotational transition lines of carbon monoxide (CO) and the molecular hydrogen (H₂) abundance. Using the outputs of Illustris-TNG cosmological simulations, we populate molecular gas clouds of unresolved sizes in individual simulated galaxies, where the effect of the interstellar radiation field with dust attenuation is also taken into account. We then use the publicly available code DESPOTIC to compute the CO line luminosities and H₂ densities without assuming the CO-to-H₂ conversion factor (α_{CO}). Our method allows us to study the spatial and kinematic structures traced by CO(1-0) and higher transition lines. We compare the CO luminosities and H₂ masses with recent observations of galaxies at low and high redshifts. Our model reproduces well the observed CO-luminosity function and the estimated H₂ mass in the local Universe. About ten percent of molecules in the Universe reside in dwarf galaxies with stellar masses lower than $10^9 M_{\odot}$, but the galaxies are generally ‘CO-dark’ and have typically high α_{CO} . Our model predicts generally lower CO line luminosities than observations at redshifts $z \gtrsim 1-2$. We argue that the difference can be explained by the highly turbulent structure suggested for the high-redshift star-forming galaxies.

Key words: methods: numerical – galaxies: evolution – ISM: molecules

1 INTRODUCTION

Molecular gas clouds (MGCs) are the birthplaces of stars, and understanding the formation and the abundance of MGCs is important in the study of galaxy formation and evolution. Despite the ubiquitous existence, direct observation of H₂ molecules in the Universe is severely limited. Radiation from H₂ molecules in the cold inter-stellar medium (ISM) is not observable because of the high excitation energies. Rotational transition lines of CO molecules are often used as a proxy for H₂ in the ISM. CO is the second most abundant molecules in the Universe, and a variety of emission lines can be observed in radio to submillimetre bands.

The rotational transition line from the state of $J = 1$ to 0, CO(1-0), is thought to trace the surface density of H₂, and the conversion factor α_{CO} between them is often assumed to be constant (see Section 4.1). However, it is also known that the value of α_{CO} varies depending on locations in a galaxy, galactic types and redshifts (e.g. Bolatto et al. 2013). Also there are many ‘CO-dark’ MGCs, where CO(1-0) emission is significantly weaker than expected for the estimated H₂ density. The variation of α_{CO} likely reflects differences in the local environments and physical properties among different MGCs, such as their column densities, intensity of far-ultraviolet (FUV) radiation

fields, dust and metal abundances (e.g. Narayanan et al. 2012; Li et al. 2018, see also Section 2).

Theoretical studies have been hampered by difficulties associated with the thermal and chemical structure and evolution of MGCs. Since most H₂ molecules are formed on the surface of dust grains, one needs to model the formation, growth and destruction of dust grains that involve various physics and chemistry even at microscopic levels. In addition, as shown in radiative transfer simulations of Glover et al. (2010), the H₂ abundance can be large in central regions of MGCs that are self-shielded against external radiation fields, which means that calculating molecular abundances needs detailed radiative transfer computations with resolving the small-scale internal structure. The conditions are simpler for CO molecules. Formation of CO does not rely on dust grains, although it needs H₂ (e.g. Krumholz 2017; Girichidis et al. 2020). The self-shielding effect of CO is less important than H₂. In addition, metallicity gradients in galaxies can enhance the inhomogeneity of the abundance ratios. These facts actually suggest that the abundance ratio between H₂ and CO may not be uniform. Numerical simulations aimed at predicting accurately the molecular abundances and line emissivities are generally required to have extremely high resolutions and to implement molecular chemistry, radiation transfer and dust models; Glover et al. (2010) and Grassi et al. (2014) study the convergence with respect to resolutions in their detailed radiative transfer simulations.

Because formation of molecules does not alter the gravitational

* E-mail: shigeki.inoue@nao.ac.jp

assembly nor overall dynamical evolution of galaxies, often post-processing methods have been applied to outputs of simulations in order to compute molecular abundances. A number of studies focus on a single galaxy with sufficiently high resolution to resolve giant molecular clouds (e.g. Narayanan et al. 2012; Li et al. 2018; Vallini et al. 2018; Armillotta et al. 2020; Keating et al. 2020; Li et al. 2020). These studies treat a small number of galaxies in isolated or in cosmological simulations and thus statistical quantities such as line luminosity functions cannot be reliably determined. Also, possible redshift evolution has not been fully addressed.

Large-volume cosmological simulations are indispensable for statistical studies of galaxy *populations*, but the typically poor mass resolution achieved to date still hampers us from directly representing individual MGCs. Also it is computationally expensive to perform multi-dimensional radiation transfer for a large number of galaxies even if the mass and spatial resolutions were appropriate. Therefore, previous studies on galaxy populations utilise large-box simulations by employing simple, empirical models or semi-analytic approaches (e.g. Obreschkow et al. 2009; Lagos et al. 2011; Popping et al. 2015; Schäbe et al. 2020; Davé et al. 2020). Popping et al. (2019) apply a post-processing method to the results of a cosmological simulation and of a semi-analytic model based on a fit to H₂ fraction obtained by Gnedin & Kravtsov (2011, also see Diemer et al. 2019). They study in detail the evolution of H₂ mass functions of galaxies from redshift $z = 0$ to 5. The derived H₂ masses are in agreement with observations of local CO-luminosity functions assuming a constant α_{CO} . However, their results predict H₂ masses that are significantly smaller than high-redshift CO observations if they adopt the same α_{CO} . As a possible reason, they argue that α_{CO} may decrease with redshift on average in the observed galaxies.

It seems that theoretical studies tend to focus on H₂ as it is more directly linked to star formation (SF). Unfortunately, H₂ is not readily observable, and thus modelling CO formation is necessary to make direct comparison with observations. It is also important to study higher rotational transition. Although high-redshift observations of CO lines are currently performed by Atacama Large Millimeter/submillimeter Array (ALMA), redshifted CO(1-0) lines from distant galaxies shift to outside the observable wavelength range of ALMA. The current high-redshift CO observations, therefore, rely on high- J transition lines, which are often converted to derive expected CO(1-0) emission with *assuming* some certain spectral line energy distribution (see Section 4.2.1).

In this paper, we propose a physical model of MGC formation and distribution, and compute H₂ density and CO line luminosity in a consistent manner. We apply the post-processing method to the outputs of a large-box cosmological simulation. Our model allows us to calculate intensities of not only CO(1-0) but also high- J lines. We make direct comparison between the simulation and observations without converting CO luminosity to H₂ density, and (dis)agreement between them could help us to understand differences of ISM and cloud properties among galaxies and their evolution with redshift.

In the rest of the present paper, Section 2 describes the simulation we utilise, our modellings for gas clouds and related parameters. Section 3 gives our computations to obtain molecular abundances and line intensities. Section 4 presents our results and comparison with recent survey observations for nearby and distant galaxies. Section 5 discusses agreement and disagreement between our results and observations. There, we address possible redshift-evolution of molecular clouds in the Universe. Section 6 summarises our findings.

2 MODELLING METHODS

Our method is based on post-processing a large-volume cosmological simulation. We aim at obtaining the large-scale distribution of galaxy populations as well as resolving spatial and kinematic structures of gas, stars and dark matter in individual galaxies. Unfortunately, even state-of-the-art cosmological simulations do not fully resolve the distribution of stars and gas clouds at length scales of $\lesssim 100$ pc. We thus resort to applying a physically motivated model to populate the galaxies with MGCs. In Section 3, we compute the molecular abundance and atomic/molecular line emissivities using approximate radiation transfer with chemistry for individual MGCs. To this end, we also need to estimate strength of radiation affecting molecular abundances of the gas clouds, and we employ simple models for radiation fields and dust attenuation.

2.1 Cosmological simulation

We utilise the data set of IllustrisTNG simulations (Nelson et al. 2018a). The details of the simulations are presented on the IllustrisTNG project web site¹ and in related papers such as Nelson et al. (2018a), Weinberger et al. (2017) and Pillepich et al. (2018). We specifically use the outputs of TNG100-1 run. The simulation box has a comoving side length of 75 Mpc, and the mass-resolutions for dark matter and gas are 7.5 and $1.4 \times 10^6 M_{\odot}$. In the simulation, dense gas cells with $\rho_{\text{cell}} > n_{\text{H,SF}} = 0.1 \text{ cm}^{-3}$ are converted to stellar particles according to a stochastic SF model. Therefore the stellar mass resolution is roughly the same as that of the parent gas cells.

The star formation rate (SFR) is calculated as

$$\dot{m}_{\text{star}} = f_{\text{M}} \frac{m_{\text{cell}}}{t_{\text{SF}}} \quad (1)$$

where m_{cell} is a mass of the parent cell, the factor f_{M} is the mass fraction of cold gas (see Section 2.2), and $t_{\text{SF}} = (G\rho_{\text{cell}})^{-1/2}$. The ISM model of Yepes et al. (1997, see also Springel & Hernquist 2003) is adopted to the star-forming gas with $\rho_{\text{cell}} > n_{\text{H,SF}}$. Type-II supernovae (SNe) are triggered immediately following the SF, and a mechanical feedback model of Springel & Hernquist (2003) is adopted to represent stellar feedback effects. Type-Ia SNe and asymptotic giant branch stars eject mass and metals into nearby gas cells. The simulation also implements creation and feedback of black holes (Springel et al. 2005) and magnetic fields (Pakmor et al. 2014).

Gravitationally bound structures are identified with the friend-of-friend and SUBFIND grouping algorithms (e.g. Springel et al. 2001). The total masses and line luminosities are computed for each SUBFIND group (galaxy).

2.2 Populating molecular gas clouds

We first need to determine the mass distribution of MGCs and their physical properties. We achieve this by using the quantities of individual gas cells in the simulation as follows. In the IllustrisTNG simulations, the ISM model of Yepes et al. (1997) is applied to gas with $\rho_{\text{cell}} > n_{\text{H,SF}} = 0.1 \text{ cm}^{-3}$. The dense gas is assumed to consist of cold and hot phases; the hot gas can cool and be converted to the cold gas by thermal instability, and the cold gas triggers "unresolved" SF and SNe. The SNe evaporate some amount of cold gas back to hot one, and the ejecta is turned into the hot phase. By considering the pressure equilibrium, the two-phase ISM model yields

¹ <https://www.tng-project.org/>

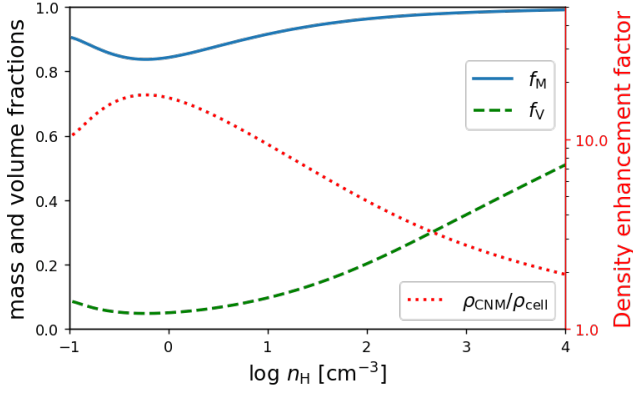


Figure 1. We plot the fractions of CNM as a function of the gas density. *Blue solid line:* the mass fraction of CNM of a gas cell at $z = 0$, which is computed by the two-phase ISM model using the same cooling function as that of IllustrisTNG simulation. *Green dashed line:* the volume fraction of CNM, which is computed by equation (2) assuming the density contrast $\phi = 100$. *Red dotted line with the right ordinate:* density enhancement factor $\rho_{\text{CNM}}/\rho_{\text{cell}} = f_{\text{M}}/f_{\text{V}}$. Note the logarithmic scales.

a barotropic equation of state (EOS). Since this effective EOS is significantly harder than the isothermal EOS, the two-phase ISM model in cosmological simulations tend to prevent galactic discs from fragmenting and forming giant clumps (Inoue & Yoshida 2019).

The two-phase ISM model computes the mass fraction of the cold-phase gas for each gas cell, f_{M} , as a function of density for a given cooling function. Typically $f_{\text{M}} \gtrsim 0.8$ for all densities above $n_{\text{H,SF}}$ and approaches asymptotically to $f_{\text{M}} \approx 1$ at high densities (see the blue solid line in Fig. 1). Thus, the cold-phase gas is dominant in mass in star-forming regions.

Wolfire et al. (1995) show that there exist two equilibrium states for a neutral gas at a given pressure, corresponding to warm and cold neutral media (WNM and CNM). They also find that the density contrast between the two phases is always $\phi \equiv \rho_{\text{CNM}}/\rho_{\text{WNM}} \sim 100$, and hardly depends on the physical properties of the gas nor on external radiation. We thus assume $\phi = 100$ in our model. Following Diemer et al. (2019) and Popping et al. (2019), we assume that all the gas in cells with $\rho_{\text{cell}} > n_{\text{H,SF}}$ is neutral (atomic and molecular), whereas the gas in cells with $\rho_{\text{cell}} < n_{\text{H,SF}}$ is fully or partly ionised and contains no molecules. For the dense gas, the total cell mass is given by $m_{\text{cell}} = m_{\text{CNM}} + m_{\text{WNM}} = \rho_{\text{CNM}}V_{\text{CNM}} + \rho_{\text{WNM}}V_{\text{WNM}}$ and volume $V_{\text{cell}} = m_{\text{cell}}/\rho_{\text{cell}} = V_{\text{CNM}} + V_{\text{WNM}}$, where V_{WNM} and V_{CNM} are the volumes of WNM and CNM within the cell. We assume that the hot and cold phases defined in the two-phase ISM model correspond to the WNM and CNM in Wolfire et al., and compute the density and volume of the CNM. The CNM volume fraction is

$$f_{\text{V}} \equiv \frac{V_{\text{CNM}}}{V_{\text{cell}}} = \frac{f_{\text{M}}}{(1 - f_{\text{M}})\phi + f_{\text{M}}}, \quad (2)$$

where $f_{\text{M}} = m_{\text{CNM}}/(m_{\text{CNM}} + m_{\text{WNM}})$. Fig. 1 shows f_{V} as a function of density. In spite of the dominance in mass (the blue solid line), CNM occupies a small volume at $\rho_{\text{cell}} \lesssim 10^2 \text{ cm}^{-3}$ when $\phi = 100$. The density enhancement factor is defined as

$$\frac{\rho_{\text{CNM}}}{\rho_{\text{cell}}} = \frac{f_{\text{M}}}{f_{\text{V}}} \quad (3)$$

which is shown by the red dotted line in Fig. 1. We assume that molecules are formed only in CNM.

Next, we need to determine the physical size of a MGC. Molecules

can be photo-dissociated by the inter-stellar radiation field (ISRF) but the dissociating radiation cannot penetrate deep into the innermost regions if the gas column density is high enough for self- and/or dust-shielding against the ISRF. The degree of the shielding effects is determined by the MGC size and density. Jeans length λ_{J} is often used to approximate the characteristic size of a MGC. We assume that a cloud in the CNM has a radius

$$r_{\text{cloud}} = \frac{\lambda_{\text{J}}}{2} = \frac{1}{2} \sqrt{\frac{\gamma P_{\text{CNM}}}{G \rho_{\text{CNM}}^2}}, \quad (4)$$

where G is gravitational constant and $\gamma = 5/3$ is the adiabatic index. Note that our base model does not consider turbulent nor magnetic pressure (although see discussion Section 5.2). Assuming the pressure equilibrium between CNM and WNM, the pressure of CNM is equal to that of the cell, i.e. $P_{\text{CNM}} = P_{\text{cell}}$. The mass and the column density of a single cloud are given by

$$m_{\text{cloud}} = \rho_{\text{CNM}}V_{\text{cloud}} = \frac{4\pi}{3} \rho_{\text{CNM}} r_{\text{cloud}}^3 \quad (5)$$

and

$$\Sigma_{\text{cloud}} = \frac{m_{\text{cloud}}}{\pi r_{\text{cloud}}^2} = \frac{4}{3} \rho_{\text{CNM}} r_{\text{cloud}}. \quad (6)$$

The above quantities of ρ_{CNM} and Σ_{cloud} are used as parameters when we compute molecular abundances and emissivities in Section 3.1.

2.3 Inter-stellar radiation field

Molecular line emission is powered by an internal or external radiation. To estimate the ISRF strength, we use a simple parametric model and calibrate it to match available observations. FUV radiation is most relevant for photo-dissociation of molecules, which is mainly emitted from young massive stars. We assume that the unattenuated ISRF intensity, χ_{int} , scales with the total SFR within a galaxy as

$$\chi_{\text{int}} = \chi_{\odot} \frac{\dot{M}_{\text{star}}}{1 M_{\odot} \text{ yr}^{-1}}, \quad (7)$$

where χ_{\odot} is the ISRF intensity in the solar neighbourhood.

To calculate the dust-attenuated ISRF, we estimate the amount of dust within a radius characterised by the SFR distribution since FUV radiation is primarily contributed by local SF in the galaxy. The dust column density is approximated to be

$$\Sigma_{\text{dust}} = \frac{f_{\text{dust}} M_{\text{metal}}(< r_{\text{SFR}})}{\pi r_{\text{SFR}}^2}, \quad (8)$$

where r_{SFR} is the three-dimensional radius within which half the total SFR of the galaxy is enclosed, $M_{\text{metal}}(< r_{\text{SFR}})$ is the total metal mass within r_{SFR} , and we assume a constant dust-to-metal fraction to be $f_{\text{dust}} = 0.3$ in our fiducial case. Assuming the typical size and solid density of a dust grain to be $a = 0.01 \mu\text{m}$ and $s = 3.0 \text{ g cm}^{-3}$, the optical depth is approximately given by

$$\tau = \frac{3 \Sigma_{\text{dust}}}{4 a s}. \quad (9)$$

Note that the dust attenuation we consider here is different from dust-shielding within a MGC. Later in Section 3.1, we discuss the dust-shielding effect on molecular emission.

In addition to the ISRF, there may exist external radiation such as the cosmic background radiation. Its intensity χ_{ext} is uniform but may vary with redshift. We follow the analytic model of Puchwein et al. (2019) and set the intensity at wavelength of 1000 as $\log(\chi_{\text{ext}}/\chi_{\odot}) \approx$

−3.0 at $z = 0$. The background intensity monotonically increases to −1.0 at $z = 6$.²

Finally, the radiation intensity in a galaxy is modelled as

$$\chi_{\text{cloud}} = \chi_{\text{int}} \exp(-\tau) + \chi_{\text{ext}}, \quad (10)$$

and this is another parameter of the molecular computations in Section 3.1. Our model assumes a constant χ_{cloud} to all the MGCs in a single galaxy. This approximation may not represent accurately local variations of molecular abundances in, for instance, spiral arms and inter-arm regions in a galaxy. We focus on the statistical quantities such as line luminosity functions for populations of galaxies in the present paper. Detailed radiative transfer within clumpy galaxies will be a subject of our future study.

3 COMPUTATIONS FOR MOLECULAR ABUNDANCES AND EMISSION

3.1 Creating look-up tables

We use the radiation transfer code DESPOTIC (Derive the Energetics and SPectra of Optically Thick Interstellar Clouds, see [Krumholz 2014](#)) that can compute the abundances of various chemical species and can predict atomic/molecular line emission from a gas cloud. Here we focus on H_2 and CO molecules. DESPOTIC employs a spherical one-zone cloud model, and includes carbon chemistry network as well as various physical processes for cooling and heating of cold ISM. For a specified parameter set that describes the physical properties of a gas cloud, the code self-consistently calculates a thermal and chemical equilibrium state. It then returns the gas and dust temperatures, species' abundances and line emissivities.

The basic parameters to be input to DESPOTIC are: volume and column densities of a cloud and the ISRF intensity. For these, we use the values of ρ_{CNM} , Σ_{cloud} and χ_{cloud} derived in the previous sections. Non-thermal velocity dispersion σ of the cloud is calculated with the assumption of a marginally bound state by gravity, where the virial parameter $\alpha_{\text{vir}} \equiv 5\sigma^2 r_{\text{cloud}} / (Gm_{\text{cloud}}) = 1$ ([Heyer & Dame 2015](#), and references therein),

$$\sigma = \sqrt{\frac{3\pi G \Sigma_{\text{cloud}}^2}{20\rho_{\text{CNM}}}}. \quad (11)$$

Although considering non-thermal (turbulent) motions in DESPOTIC might appear inconsistent with the assumption made when calculating r_{cloud} (Section 2.2), we adopt the above equation by noting that MGCs can be highly turbulent after gravitational contraction. [Federrath & Klessen \(2012\)](#) demonstrate that efficient star formation is driven by compressive turbulence (see also [Federrath 2018](#)). We also note that the effect of varying r_{cloud} shall be discussed in Section 5.2. The ionization rate due to hard X-ray photons and cosmic rays is set to $\xi = 10^{-17} \chi_{\text{cloud}} \text{ s}^{-1}$ per H nucleus. We assume the dust abundance in a cloud to be proportional to its metallicity Z_{cloud} . With the efficient mixing approximation within a gas cell, we consider $Z_{\text{cloud}} = Z_{\text{cell}}$ but impose the minimum metallicity of $10^{-3} Z_{\odot}$ set by Population III stars ([Kuhlen et al. 2012](#)), where Z_{\odot} is the solar metallicity. The dust abundance of the cloud is given as

$$D_{\text{cloud}} = D_{\text{MW}} \frac{Z_{\text{cloud}}}{Z_{\odot}}, \quad (12)$$

² The values of $\log(\chi_{\text{ext}}/\chi_{\odot}) \approx -2.0, -1.5, -1.3, -1.1$ and -1.0 at redshifts $z = 1, 2, 3, 4$ and 5 , respectively.

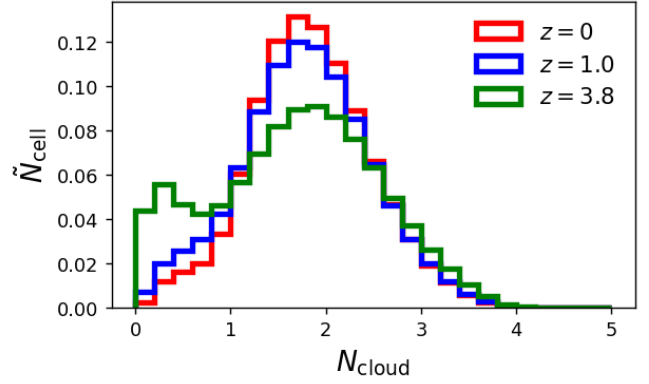


Figure 2. Normalised histograms of gas cells as functions of N_{cloud} computed by equation (13) in the snapshots at redshifts $z = 0, 1.0$ and 3.8 .

where D_{MW} is the Milky Way dust abundance. We adopt the total abundance of $[\text{C}/\text{H}] = 2 \times 10^{-4} Z_{\text{cloud}}/Z_{\odot}$, $[\text{O}/\text{H}] = 4 \times 10^{-4} Z_{\text{cloud}}/Z_{\odot}$ and $[\text{M}/\text{H}] = 2 \times 10^{-7} Z_{\text{cloud}}/Z_{\odot}$ for C, O and the other refractory metals (M), respectively.³ These abundances are consistent with the solar value for $Z_{\text{cloud}} = Z_{\odot}$ ([Draine 2011](#)). For dust grains, we set three cross sections per H nucleus: one for thermal radiation $\sigma_{10} = 2 \times 10^{-25} \text{ cm}^{-2}$ at 10 K, one for photoelectric heating $\sigma_{\text{PE}} = 10^{-21} \text{ cm}^{-2}$ and yet another one for ISRF $\sigma_{\text{ISRF}} = 3 \times 10^{-22} \text{ cm}^{-2}$. The dust-gas coupling coefficient is set to $\alpha_{\text{gd}} = 3.2 \times 10^{-34}$. The spectral index for dust thermal radiation is $\beta = 2.0$. Finally, the cosmic microwave background temperature is $T_{\text{CMB}} = 2.73 \text{ K}$ at $z = 0$.

With these settings, DESPOTIC needs five parameters: ρ_{CNM} , Σ_{cloud} , χ_{cloud} , Z_{cloud} and z . Since Σ_{cloud} is a function of ρ_{CNM} in the two-phase ISM model used in Illustris-TNG and the cloud size $r_{\text{cloud}} = \lambda_1/2$ depends only on ρ_{CNM} at a given z , we generate a look-up table of H_2 fractions f_{H_2} and line emissivities W_{CO} as a function of ρ_{CNM} , χ_{cloud} and Z_{cloud} at each output epoch (redshift). The parameter space covers the values of the three quantities with 30, 10 and 10 grids for ρ_{CNM} , χ_{cloud} and Z_{cloud} in logarithmic spacing.

3.2 Integrating the clouds

Using the look-up table, we compute CO line intensities and H_2 abundance for each gas cell according to the procedures described in Section 2.2. We do not consider inter-galactic components that are not gravitationally bound to any galaxies, because such a warm/hot, diffuse gas is highly ionised and contains little molecules.

The number of clouds in a gas cell is given by

$$N_{\text{cloud}} = \frac{V_{\text{CNM}}}{V_{\text{cloud}}} = \frac{m_{\text{CNM}}}{m_{\text{cloud}}}. \quad (13)$$

We allow this value to be less than 1, i.e. a computational cell covers only a fraction of a MGC. Histograms in Fig. 2 illustrate the distribution of gas cells as functions of N_{cloud} in the snapshots at $z = 0, 1.0$ and 3.8 . The majority of the cells have $N_{\text{cloud}} \sim 2$ in all of the snapshots although the fraction of cells with $N_{\text{cloud}} < 1$ somewhat

³ Although these values can be directly read from the snapshot data of Illustris-TNG, we assume the simple scaling with metallicity to reduce the number of input parameters. The actual abundances in the simulation do not significantly deviate from the scaling relations.

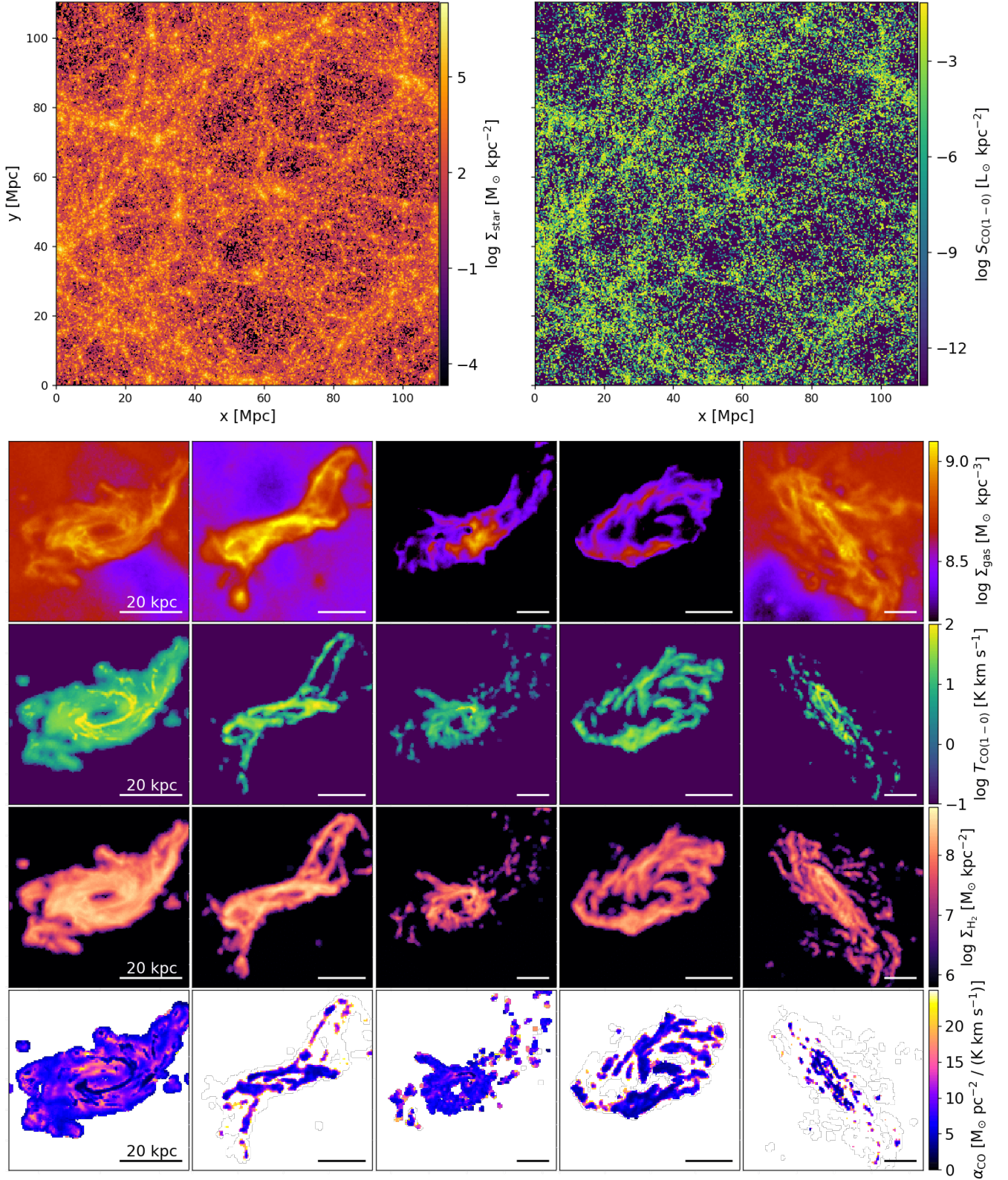


Figure 3. The large-scale distribution and the structure of galaxies. *Top two panels:* stellar mass (left) and CO(1-0) luminosity (right) distributions in the whole simulation box of the TNG100-1 at $z = 0$. *Bottom set of panels:* the five brightest galaxies in CO(1-0) luminosity in the simulation (from left to right for the first to fifth brightest ones). From top to bottom, the panels show gas surface densities, velocity-integrated surface brightness temperatures in CO(1-0), H₂ surface densities and local α_{CO} , respectively. The galaxies are oriented in random directions. The horizontal bar on the bottom right corner in each panel indicates the physical scale of 20 kpc.

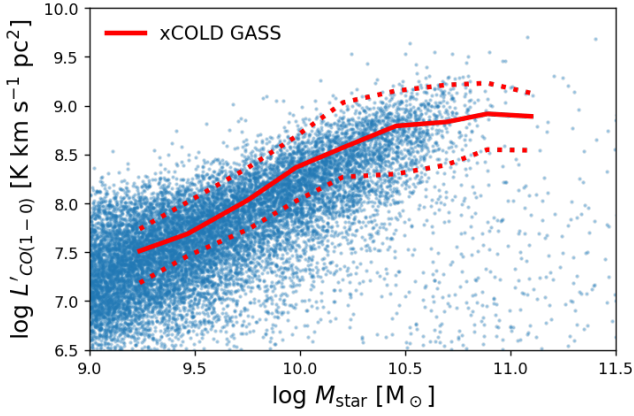


Figure 4. Velocity-integrated brightness temperatures of CO(1-0) lines of galaxies as functions of stellar mass. The blue dots indicate our results using TNG100-1 at $z = 0$. The red solid and dashed lines show the median and the $\pm 1\sigma$ ranges of the xCOLD GASS sample with detection of the CO(1-0) lines.

increases at $z = 3.8$. By calculating a velocity-integrated line emissivity W in a manner described in Section 3.1, we obtain the line intensity as $I_{\text{cloud}} = \pi r_{\text{cloud}}^2 W$. Then, the total intensity of a gas cell is simply

$$I_{\text{cell}} = I_{\text{cloud}} N_{\text{cloud}}. \quad (14)$$

The total H_2 mass is $m_{\text{H}_2, \text{cell}} = f_{\text{H}_2} m_{\text{CNM}}$, where f_{H_2} is mass fraction of H_2 with respect to all the components including hydrogen, helium and heavy elements. We note that introducing N_{cloud} in Equation (13) enables our model to be independent of the mass-resolution of a simulation.

4 RESULTS

4.1 Galaxies in the local Universe

We begin with testing our model prediction at $z = 0$ by comparing with observations of local galaxies. The top two panels in Fig. 3 show the large-scale distribution of stellar mass (left) and velocity-integrated CO(1-0) luminosity. The filamentary cosmic web can be seen clearly in not only the stellar distribution but also the CO(1-0) emission. The bottom set of panels show, for the five CO-brightest galaxies, the surface gas density, CO(1-0) brightness temperature $T_{\text{CO}(1-0)}$, H_2 surface density, and $\alpha_{\text{CO}} = \Sigma_{\text{H}_2}/T_{\text{CO}(1-0)}$. These CO-brightest galaxies have *local* values of $\alpha_{\text{CO}} \sim 5\text{--}10$. We find approximately uniform α_{CO} in regions where CO(1-0) line is strong. Note, however, that our model does not incorporate the local variation of ISRF within a galaxy (see Section 2.3).

4.1.1 Comparison with xCOLD GASS

The xCOLD GASS survey (Saintonge et al. 2017) has observed CO emission of local galaxies and built a large sample that is unbiased except for sampling with an equal frequency among stellar mass bins between $M_{\text{star}} = 10^9$ and $10^{11.5} M_{\odot}$. We compare our model prediction with their observations. Fig. 4 shows galaxy-integrated brightness temperatures of CO(1-0) lines as a function of stellar mass. The blue dots indicate results (galaxies) from our model, and the red lines delineate the median (solid) and $\pm 1\sigma$ deviations (dotted) for

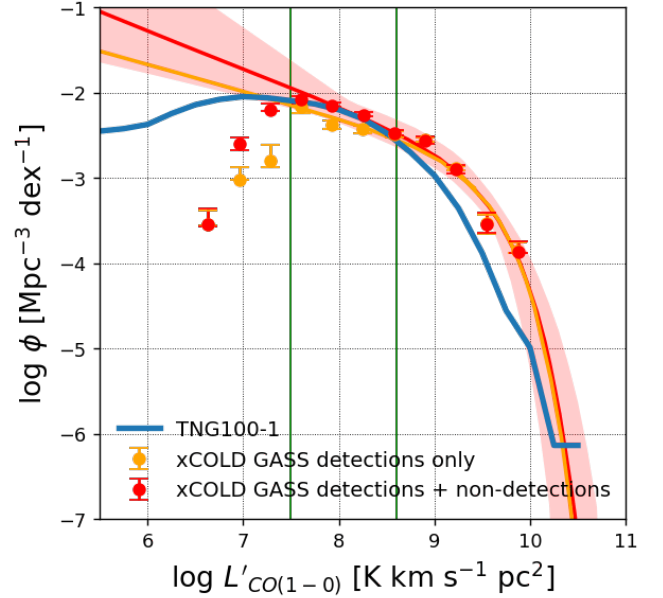


Figure 5. LFs of CO(1-0) lines at $z = 0$. The blue solid line delineates our result using TNG100-1. The filled circles with error bars indicate the observations of xCOLD GASS. The yellow ones include all observed sample, but the red ones only include those with detections of CO(1-0). The yellow and red solid lines are their fittings with Schechter functions. The vertical green lines at $\log L'_{\text{CO}(1-0)} = 7.5$ and 8.6 indicate the completeness limits of xCOLD GASS due to their stellar mass cut and their gas fraction integration limit, respectively.

the observed sample with CO(1-0) line detection. Clearly, our model reproduces the correlation of $L'_{\text{CO}(1-0)}$ with M_{star} , in agreement with the xCOLD GASS sample. The $L'_{\text{CO}(1-0)}\text{--}M_{\text{star}}$ relation is thought to correspond to the SF main sequence, i.e. correlation between galactic SFRs and M_{star} . Galaxies with high SFRs are molecular-rich and therefore bright in CO emission.

Fig. 5 compares CO-luminosity functions (LFs) between our model and xCOLD GASS. Again, the result is consistent with the observed CO-LFs, with the model underpredicting slightly in the range of $L'_{\text{CO}(1-0)} \sim 10^9\text{--}10^{10} \text{ K km s}^{-1} \text{ pc}^2$. Below the completeness limit due to the stellar mass cut of xCOLD GASS at $\log L'_{\text{CO}(1-0)} \lesssim 7.5$, the CO-LF predicted by our model decreases and significantly deviates from the extrapolation of the Schechter functions fitted to the observations. Also in the low-luminosity range, the data points of xCOLD GASS indicate lower number density than our model. This could be attributed to the stellar mass cut of xCOLD GASS, whereas our model does not impose such a lower limit of stellar mass on our galaxy sampling.

Fig. 6 shows galaxy-integrated line ratios of $r_{21} \equiv L'_{\text{CO}(2-1)}/L'_{\text{CO}(1-0)}$ as a function of M_{star} . All the simulated galaxies are located in the range between $\log r_{21} \approx -1$ and 0, and cover the distribution of most of the galaxies observed in xCOLD GASS in the range of $M_{\text{star}} \gtrsim 10^9 M_{\odot}$. Interestingly, below the stellar mass limit of xCOLD GASS, i.e. in $M_{\text{star}} < 10^9 M_{\odot}$, our result predicts that most of the low-mass galaxies have low ratios of $\log r_{21} \approx -0.8$. The combination of our model and the IllustrisTNG simulation can be tested by future high-sensitivity observations.

Hereafter, we re-define α_{CO} as a galaxy-integrated value: $\alpha_{\text{CO}} \equiv M_{\text{H}_2}/L'_{\text{CO}(1-0)}$. We note that α_{CO} in the bottom panels of Fig. 3 is

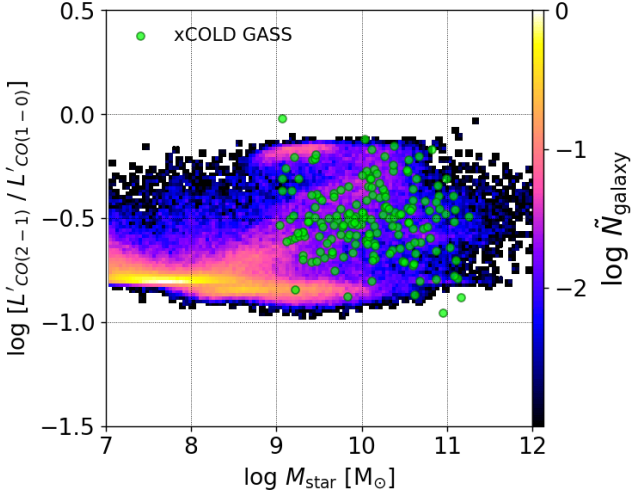


Figure 6. The line luminosity ratios $L'_{\text{CO}(2-1)}/L'_{\text{CO}(1-0)}$ against stellar mass. The colour indicates the number of galaxies in each bin normalised to the highest value (see the colour bar on the right). The green filled circles are the observed values of the xCOLD GASS sample.

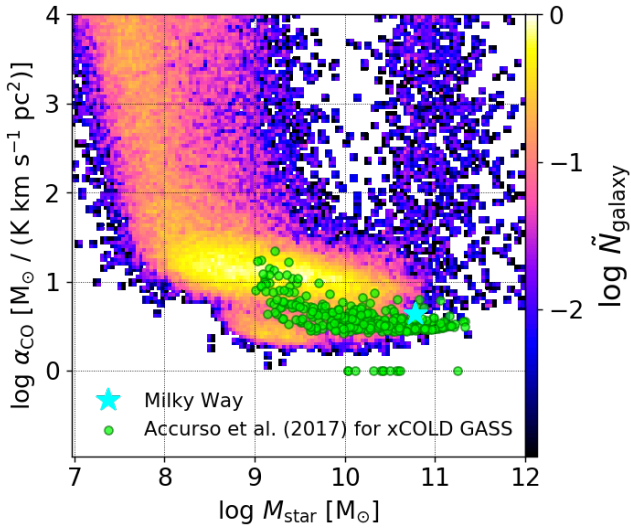


Figure 7. Distribution of galaxy-integrated α_{CO} and stellar mass in TNG100-1. The colour code is the same as in Fig. 6. To ensure the accuracy of α_{CO} , we here exclude the galaxies whose total masses of star-forming gas are lower than $10^7 M_{\odot}$. The cyan symbol at $(\log M_{\text{star}}, \log \alpha_{\text{CO}}) = (10.8, 0.63)$ corresponds to the values measured in the inner Galactic disc. The green filled circles are α_{CO} estimated using a model of Accurso et al. (2017) for the xCOLD GASS sample.

defined as the ratio of surface H_2 mass density to $\text{CO}(1-0)$ brightness temperature measured locally. Fig. 7 shows the distribution of α_{CO} and galactic stellar masses. We find α_{CO} is approximately constant at $\log \alpha_{\text{CO}} \approx 1$ in the range of $M_{\text{star}} \sim 10^8 - 10^{10.5} M_{\odot}$. However, α_{CO} increases below $M_{\text{star}} \sim 10^8 M_{\odot}$, and there is a population of massive galaxies that have high α_{CO} with $M_{\text{star}} \gtrsim 10^{11} M_{\odot}$. These low- and high-mass galaxies with such high α_{CO} correspond to dwarf and massive elliptical galaxies, and their high α_{CO} are because of their low metallicities and/or diffuse gas distribution (see Section 4.1.2).

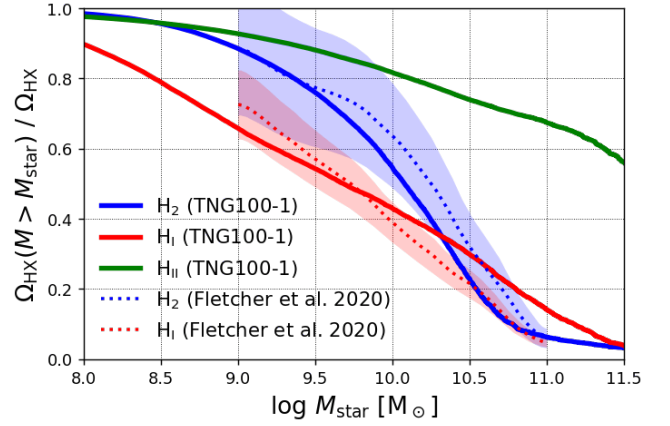


Figure 8. The fractions of H_2 (blue), H_I (red) and H_{II} (green) that reside in galaxies above a given M_{star} . The solid lines indicate our results. The dotted lines are the observational results of Fletcher et al. (2020) derived from the xCOLD GASS (blue dotted) and xGASS (red dotted) surveys, and the shaded regions show their observational 1σ errors.

In Fig. 7, the cyan star-shaped symbol indicates $\alpha_{\text{CO}} = 4.3$ measured in the Galactic inner disc (Bolatto et al. 2013) with the Galactic stellar mass of $M_{\text{star}} = 6.08 \times 10^{10} M_{\odot}$ (Licquia & Newman 2015). The green filled circles correspond to the xCOLD GASS sample where α_{CO} are not observationally determined but estimated using the model of Accurso et al. (2017).⁴ These values of α_{CO} appear to be somewhat lower than the averaged values in our model although these are within the range covered by our prediction.

From our model, we can compute not only mass of H_2 but also those of H_I and H_{II} . We assume that the star-forming gas is neutral. In such a gas cell, WNM is assumed to be fully atomic, and abundances of H_2 and H_I in CNM are computed with DESPOTIC.⁵ We consider the diffuse gas with $\rho_{\text{cell}} < n_{\text{H,SF}}$ to form no molecules, and its ionised fraction is computed in the IllustrisTNG simulation. Note again that we do not take into account inter-galactic gas that is not bound to any galaxies. Using these quantities, we estimate the cosmic densities of hydrogen in molecular, atomic and ionised states to be $\Omega_{\text{H}_2} = 6.44 \times 10^{-5} h^{-1}$, $\Omega_{\text{H}_I} = 4.13 \times 10^{-4} h^{-1}$ and $\Omega_{\text{H}_{\text{II}}} = 4.79 \times 10^{-3} h^{-1}$, respectively. In observations, Fletcher et al. (2020) estimates $\Omega_{\text{H}_2} = (5.34 \pm 0.47) \times 10^{-5} h^{-1}$ from xCOLD GASS and $\Omega_{\text{H}_I} = (2.35^{+2.17}_{-0.67}) \times 10^{-4} h^{-1}$ from the xGASS survey (Catinella et al. 2018). Jones et al. (2018) determine $\Omega_{\text{H}_I} = (3.8 \pm 0.7) \times 10^{-4} h^{-1}$ from the ALFALFA survey (Giovanelli et al. 2005). The values of Ω_{H_2} and Ω_{H_I} in our model are thus consistent with these observational measurements although Ω_{H_2} is slightly above the error range of the xCOLD GASS observations. Fig. 8 shows fractions of the cosmic hydrogen densities cumulated from galaxies with high M_{star} . The fractions of Ω_{H_2} in our model is consistent with the observations of Fletcher et al. (2020) within the error ranges although those of Ω_{H_I} appear to be somewhat higher than the observations in $M_{\text{star}} \gtrsim 10^{10.5} M_{\odot}$. As Fletcher et al. (2020) mention, our results show that nearly ninety per cent of H_2 in the Universe resides in galaxies with $M_{\text{star}} > 10^9 M_{\odot}$, and dwarf galaxies do not host a significant

⁴ The model of Accurso et al. (2017) gives α_{CO} as a function of metallicity and offset from the SF main sequence.

⁵ Although DESPOTIC also computes H_{II} abundance in a MGC, an amount of H_{II} is generally negligible.

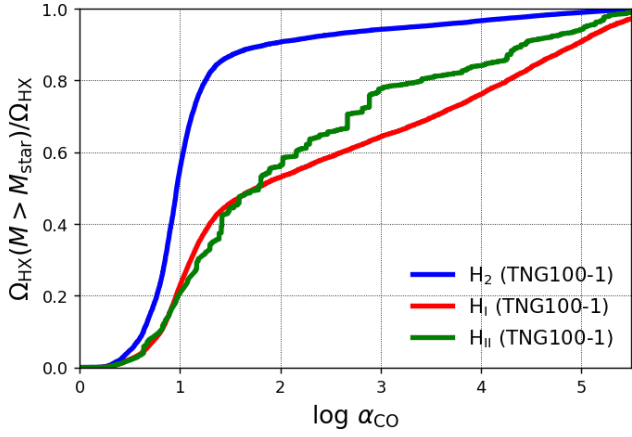


Figure 9. Same as Fig. 8 but for the fractions of hydrogen that resides in galaxies below a given α_{CO} .

amount of molecules. However, it is worth reminding of the fact that the observed H_2 mass is estimated from CO luminosity via α_{CO} of Accurso et al. (2017); on the other hand, our model directly computes H_2 mass. It is known that dwarf galaxies generally have low SF efficiencies leading to low stellar mass to halo mass ratios (e.g. Behroozi et al. 2013a,b, 2019), and it is often attributed to intense gas outflows by SNe due to their shallow potentials. From our result in Fig. 8, we argue that the low H_2 abundances in the low-mass galaxies could be another cause of the low SF efficiencies of dwarfs.

Fig. 9 shows the fractions of the cosmic hydrogen densities summed over galaxies with low α_{CO} in our model. Nearly ninety per cent of H_2 gas in the Universe resides in galaxies with $\log \alpha_{\text{CO}} \approx 0.5$ – 1.5 , and only ten per cent of H_2 is formed in ‘CO-dark’ galaxies with $\log \alpha_{\text{CO}} \gtrsim 1.5$. Although such CO-dark molecular clouds in these galaxies would be missed in observations, their total amount is expected to be insignificant with respect to the total molecular mass in the Universe. However, the CO-dark galaxies host nearly half the total amounts of H I and H II .

As we show above, our model adopted to IllustrisTNG with our fiducial parameter settings can thus reproduce well the galaxy-integrated properties reported in the previous observational studies. We discuss parameter-dependence of our model in Section 5.1.

4.1.2 Other models

We find that the galaxy-integrated α_{CO} strongly correlates with the averaged metallicities Z of star-forming gas and their column densities Σ_{cloud} , whereas the correlations with the other properties such as ISRF χ_{cloud} and gas fractions are less clear. This finding is consistent with the result of Narayanan et al. (2012), in which they have proposed a fitting function obtained from their isolated and merger simulations:

$$\alpha_{\text{CO}}^{\text{fit}} = \frac{20.6}{\langle Z/Z_{\odot} \rangle \langle \Sigma_{\text{H}_2} \rangle_{\text{H}_2}^{0.5}}, \quad (15)$$

where $\langle Z/Z_{\odot} \rangle$ is mass-weighted mean of gaseous metallicity, and $\langle \Sigma_{\text{H}_2} \rangle_{\text{H}_2}$ is average of H_2 column densities weighted by H_2 mass over

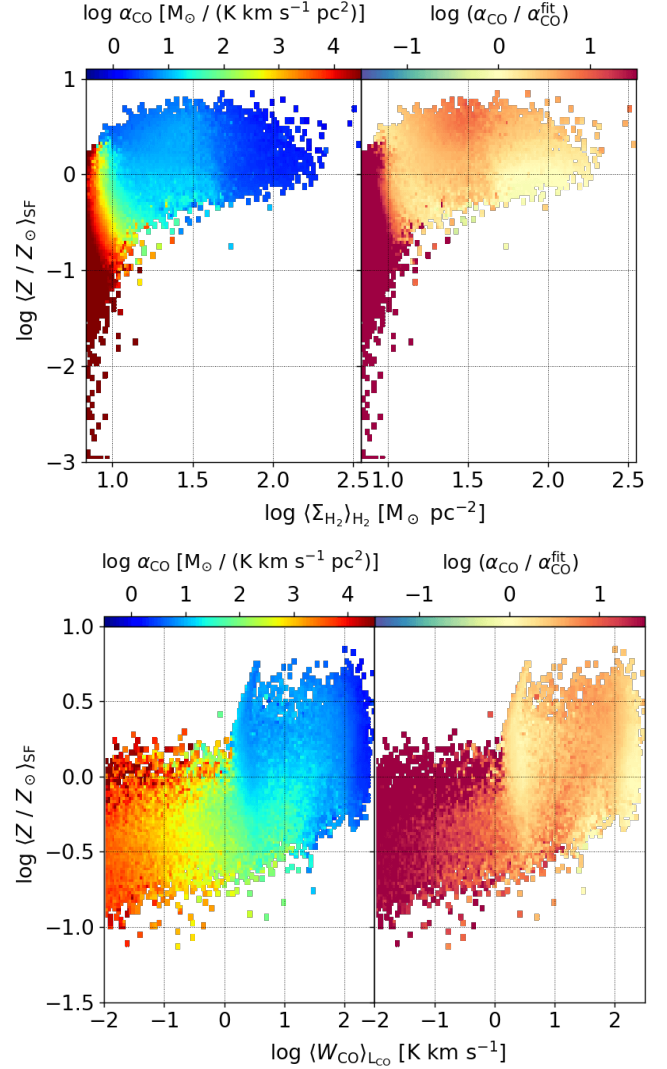


Figure 10. *Left panels:* the averaged values of $\log \alpha_{\text{CO}}$ in our model. *Right panels:* the differences of our results from the fitting functions of Equations (15 and 16); if $\log(\alpha_{\text{CO}}/\alpha_{\text{CO}}^{\text{fit}}) > 0$, our model predicts higher α_{CO} than the fitting functions. The ordinates $\langle Z/Z_{\odot} \rangle_{\text{SF}}$ indicate mass-weighted metallicities among star-forming gas cells within the galaxy. In the top panels, the abscissa $\langle \Sigma_{\text{H}_2} \rangle_{\text{H}_2}$ indicates average of H_2 column densities weighted by molecular mass over all gas clouds in the galaxy. In the bottom panels, the abscissa $\langle W_{\text{CO}} \rangle_{\text{LCO}}$ indicates average of luminosity-weighted CO emissivities over all clouds in the galaxy. We here exclude galaxies whose masses of star-forming gas are lower than $10^7 M_{\odot}$.

all gas clouds⁶ in the units of $M_{\odot} \text{pc}^{-2}$. The top panels of Fig. 10 show distribution of the ensemble averages of $\log \alpha_{\text{CO}}$ in our model and comparison with the fitting function of equation (15). In the top left panel, the mean α_{CO} increases with decreasing Z and Σ_{H_2} . Especially, most of the metal-poor galaxies with $\log \langle Z/Z_{\odot} \rangle \lesssim -0.5$ have quite high α_{CO} , and galaxies with $\langle \Sigma_{\text{H}_2} \rangle_{\text{H}_2} \lesssim 10 M_{\odot} \text{pc}^{-2}$ have high α_{CO} irrespective of their metallicities. In the top right panel, we show logarithmic differences of α_{CO} between our model and equation (15).

⁶ The definition is $\langle \Sigma_{\text{H}_2} \rangle_{\text{H}_2} \equiv \sum_i m_{\text{H}_2,i} \Sigma_{\text{H}_2,i} / \sum_i m_{\text{H}_2,i}$, where $m_{\text{H}_2,i}$ is H_2 mass in i -th gas cell, and $\Sigma_{\text{H}_2,i}$ is H_2 column density of a gas cloud in the cell: $\Sigma_{\text{H}_2} = \Sigma_{\text{cloud}} f_{\text{H}_2}$.

The values of α_{CO} are consistent between our model and the fitting function for the galaxies with $\langle \Sigma_{\text{H}_2} \rangle_{\text{H}_2} \gtrsim 10 M_{\odot} \text{ pc}^{-2}$ within a factor of unity. The fitting function, however, predicts significantly lower α_{CO} than our model for the galaxies with $\langle \Sigma_{\text{H}_2} \rangle_{\text{H}_2} \lesssim 10 M_{\odot} \text{ pc}^{-2}$. This may be because the fitting function is derived from a number of their isolated and merger simulations for relatively massive galaxies with $M_{\text{baryon}} \sim 10^{11} M_{\odot}$.

The fitting function of Equation (15) can be converted to an ‘observable form’ (Narayanan et al. 2012),

$$\alpha_{\text{CO}}^{\text{fit}} = \frac{10.7}{\langle Z/Z_{\odot} \rangle^{0.65} \langle W_{\text{CO}} \rangle_{\text{LCO}}^{0.32}}, \quad (16)$$

where $\langle W_{\text{CO}} \rangle_{\text{LCO}}$ is the luminosity-weighted mean of CO(1-0) emissivities over all clouds in a galaxy in units of K km s^{-1} . The bottom panels of Fig. 10 show the same as the top ones but with $\langle W_{\text{CO}} \rangle_{\text{LCO}}$ for the abscissas. The values of α_{CO} increase with decreasing $\langle W_{\text{CO}} \rangle_{\text{LCO}}$ in our model, and equation (16) gives significantly lower α_{CO} for galaxies with low $\langle W_{\text{CO}} \rangle_{\text{LCO}} \lesssim 1 \text{ K km s}^{-1}$. Thus, the fitting functions derived by Narayanan et al. (2012) appear to be accurate and useful for CO-bright galaxies that have dense molecular clouds with $\langle W_{\text{CO}} \rangle_{\text{LCO}} \gtrsim 1 \text{ K km s}^{-1}$ and $\langle \Sigma_{\text{H}_2} \rangle_{\text{H}_2} \gtrsim 10 M_{\odot} \text{ pc}^{-2}$.

Our model employs a simple approximation for calculating ISRF χ_{cloud} and dust opacity τ for gas clouds (Section 2.3). Narayanan et al. (2012) use dust radiation transfer calculations (Narayanan et al. 2011) for spatially resolved distribution of radiation sources such as stars and active galactic nuclei with spectrum energy distribution models. It is noteworthy that, despite the simplicity, our model reproduces their fitting results of $\alpha_{\text{CO}}^{\text{fit}}$ for a large number of galaxies in cosmological simulations except for the diffuse galaxies with $\langle \Sigma_{\text{H}_2} \rangle_{\text{H}_2} \lesssim 10 M_{\odot} \text{ pc}^{-2}$.

4.2 Results at high redshifts

We post-process snapshots of TNG100-1 at high redshifts. From the agreement of our results with the xCOLD GASS survey in Section 4.1.1, we can possibly apply our model to high-redshift galaxies without calibrating the parameters or altering our model. This may, however, be a naive expectation. For example, dust properties such as typical size a and dust-to-metal fraction f_{dust} (Sections 2.3 and 3.1) can evolve with redshift. The inaccuracy of our modelling for ISRF χ_{cloud} can be amplified since the ISRF can be more intense due to the higher SFRs and lower dust abundances (lower metallicities) of high-redshift galaxies. In addition, galactic morphologies are more irregular and complex due to intense gas accretion and frequent mergers at higher redshifts. Our modelling such as assuming $r_{\text{cloud}} = \lambda_J/2$ may no longer be accurate for such dense and irregular galaxies.

We adopt the fiducial model described in Section 2.2 to outputs of TNG100-1 from $z = 0.5$ to 3.8 without changing the parameters. In what follows, we examine (in)consistency with CO line observations at high redshifts. We note that the available observations are still limited to a small number of galaxies. Future large, systematic surveys will allow us to perform substantially better and rigorous comparison.

4.2.1 Comparison with ASPECS

We compare our results from the ASPECS surveys. Decarli et al. (2016) provide the results of their pilot observation at wavelengths of 1 and 3 mm (band 3 and 6) for galaxies at the mean redshifts $\langle z \rangle = 0.5, 1.0, 1.4, 2.6$ and 3.8. Decarli et al. (2019) present data from large-programme (LP) observations at 3 mm for galaxies at $\langle z \rangle = 0.3, 1.4, 2.6$ and 3.8, which covers a wider area than the pilot

survey. Redshifted CO(1-0) emission (rest-frame 2.6 mm line) is not covered by currently available receiver bands of ALMA. Hence, the high-redshift CO observations are aimed at detecting higher- J lines, CO[$J-(J-1)$], that have shorter rest-frame wavelengths. The ASPECS surveys observe the emission of $J = 3, 4, 2, 3$ and 4 at $z = 0.5, 1.0, 1.4, 2.6$ and 3.8, respectively; CO(5-4) is also observed at $z = 1.4$ in the pilot observation.

In our model, high- J lines are directly calculated with DESPOTIC without introducing any conversion factors. The effective survey volume of ASPECS is much smaller than the simulation box of TNG100-1. We are thus able to estimate the cosmic variance by sampling cubic regions with side lengths of 4.59, 5.18, 8.30, 6.82 and 5.48 Mpc (physical) at $z = 0.5, 1.0, 1.4, 2.6$ and 3.8, respectively. These sampling volumes are consistent with those of ASPECS pilot observation for $z = 0.5, 1.0$ and ASPECS LP for $z = 1.4, 2.6$ and 3.8. A total of 16384 cubic regions are randomly selected in the simulation box.

Fig. 11 compares high- J CO-LFs. The blue solid lines indicate our results including all the galaxies in the simulation. Our model appears to underpredict the CO-LFs for CO(5-4) at $z = 1.4$, CO(3-2) at $z = 2.6$ and CO(3-2) at $z = 3.8$. The model CO-LFs are outside the ranges of uncertainties of the ASPECS pilot and LP data.

For high-redshift galaxies, CO(1-0) line luminosity is *estimated* from the higher- J lines using the line ratios r_{J1} for an assumed line energy distribution: $L'_{\text{CO}[J-(J-1)]} = r_{J1} L'_{\text{CO}(1-0)}$. The ASPECS surveys use r_{J1} estimated by Daddi et al. (2015): $r_{J1} = 0.76, 0.42, 0.31$ and 0.23 for $J = 2, 3, 4$ and 5, respectively. Our model provides CO(1-0) line luminosities directly. Fig. 12 compares our model CO(1-0) LFs with those converted from the ASPECS data. We also plot the observational results of Orellana-González et al. (2020) which include brighter galaxies than ASPECS.⁷ Our model matches the observed CO-LFs within the error ranges at $z \lesssim 2.0$. At $z = 2.6$ and 3.8, the modelled galaxies appear to lack galaxies brighter than $L'_{\text{CO}(1-0)} = 10^9 \text{ K km s}^{-1} \text{ pc}^2$, which is clearly inconsistent with the ASPECS surveys.

The ASPECS observations assume $\alpha_{\text{CO}} = 3.6 M_{\odot} (\text{K km s}^{-1} \text{ pc}^2)^{-1}$ for all observed galaxies.⁸ Accordingly, their galaxy-integrated H_2 mass is estimated as

$$M_{\text{H}_2} = \frac{\alpha_{\text{CO}}}{r_{J1}} L'_{\text{CO}[J-(J-1)]}. \quad (17)$$

Note the estimate is subject to uncertainties of the two conversion factors: α_{CO} and r_{J1} , whereas our model can calculate M_{H_2} independently from CO line luminosity. Fig. 13 compares the model and observed (estimated) H_2 mass functions. The model agrees reasonably well with ASPECS and Orellana-González et al. (2020) at $z = 0.5, 1.0$ and 1.4. However, our model tends to overpredict M_{H_2} at $z > 2$. This trend is actually *opposite* to what is found for CO LFs. Overall, at high redshift, our model predicts lower L'_{CO} and larger M_{H_2} than ASPECS, and the discrepancy appears to be larger at higher redshift. This indicates that the average α_{CO} in our model increases with redshift. In Section 5.2, we discuss possible causes of the variation of α_{CO} and further investigate the inconsistency with the observations.

⁷ Orellana-González et al. (2020) estimate the CO-LFs for their compilation of various observations using correlations between the luminosities of radio continuum, infrared and CO emission.

⁸ Orellana-González et al. (2020) also assume $\alpha_{\text{CO}} = 3.6$.

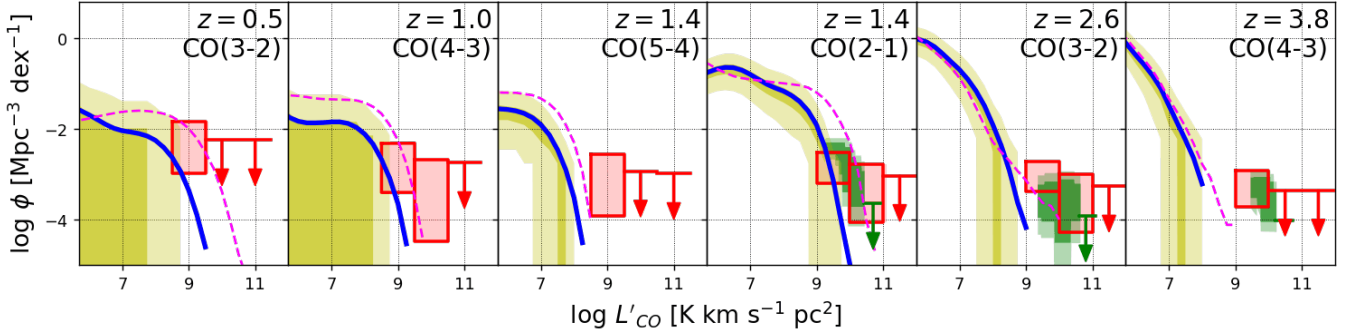


Figure 11. Luminosity functions of CO[J -($J-1$)] transition lines, where J is consistent with that of the ASPECS surveys in each panel. The blue solid lines indicate our results including all galaxies in the whole simulation box of TNG100-1. The shaded regions with thick and thin yellow are 1σ and 2σ confidence intervals of the cosmic variance computed in the volumes whose sizes are the same as the observing regions of ASPECS. The magenta dashed lines are the same as the blue solid lines but assuming the cloud sizes to be ten times larger: $r_{\text{cloud}} = 5\lambda_J$ (see Section 5.2). The red and green boxes indicate the observational determinations of the ASPECS pilot and LP (see Decarli et al. 2016, 2019), respectively. The vertical sizes of the red boxes show the Poisson errors of the pilot observation. The thick and thin green regions correspond to 1σ and 2σ confidence intervals of the LP observations. The horizontal bars with downwards arrows indicate upper limits of the observations.

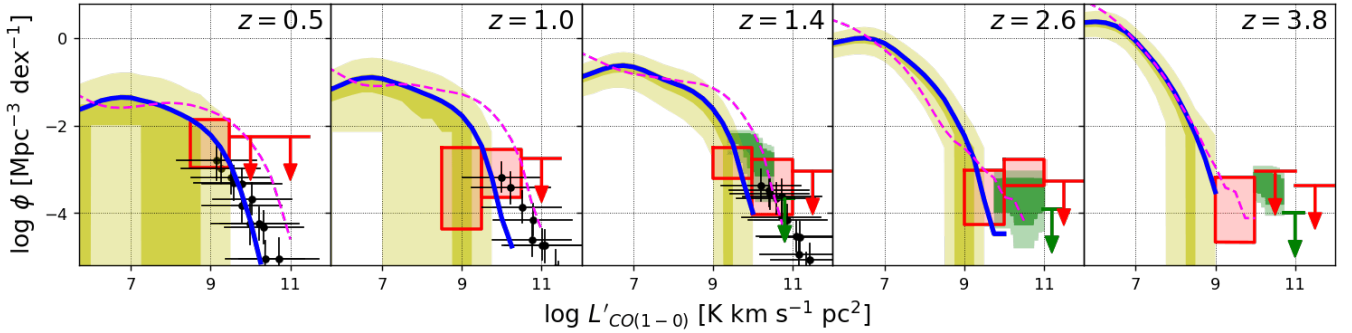


Figure 12. Same as Fig. 11 but for CO(1-0) emission. In the three panels from left, the black filled circles with error bars indicate the observational results of Orellana-González et al. (2020) at $z = 0.5, 1.1$ and 1.5 , respectively.

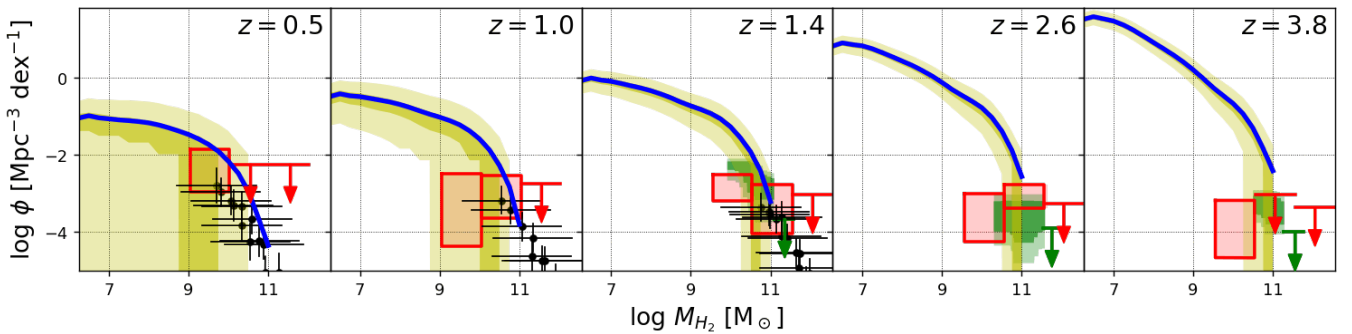


Figure 13. Same as Figs. 11 and 12 but for H_2 masses. The observations plotted here are the same as those in Fig. 12 but shifted horizontally by $\alpha_{\text{CO}} = 3.6$. The results with $r_{\text{cloud}} = 5\lambda_J$ are not shown since these are hardly different from the fiducial case.

5 DISCUSSION

5.1 Parameter calibration at $z = 0$

The results presented in Section 4.1.1 show that our model reproduces well the galaxy-integrated luminosities of CO(1-0) and the line ratios to CO(2-1) of the xCOLD GASS sample. From the consistency of

the molecular mass distribution shown in Fig. 8, we expect that α_{CO} in our model is close to those estimated for the observed galaxies (see also Fig. 7).

Since our post-processing method employs several controlling parameters described in Section 2, we discuss the dependence of our results on the parameters. In Section 2.2, we assume the density ratio

based on the two-phase ISM model with $\phi \equiv \rho_{\text{CNM}}/\rho_{\text{WNM}} = 100$, which yields the density enhancement factor of $1 < f_{\text{M}}/f_{\text{V}} \lesssim 20$. If we set $f_{\text{M}} = f_{\text{V}} = 1$, by effectively deviating from the ISM model, our results of L'_{CO} and M_{H_2} do not systematically change. Only the scatter becomes large for low-mass galaxies. This is because the most important parameter for molecular abundance in a cloud is Σ_{cloud} rather than ρ_{CNM} (e.g. Li et al. 2018). We approximate a cloud size to be $r_{\text{cloud}} = \lambda_{\text{J}}/2$, and $\lambda_{\text{J}} \propto \rho_{\text{CNM}}^{-1}$ under the pressure equilibrium between the CNM and WNM. Therefore, $\Sigma_{\text{cloud}} \propto \rho_{\text{CNM}} r_{\text{cloud}}$ is independent of the density enhancement factor, and the resulting L'_{CO} and M_{H_2} do not change significantly. In fact, we find that increasing Σ_{cloud} can make L'_{CO} considerably larger (see Section 5.2).

We employ a simple model for the unattenuated ISRF χ_{int} that is proportional to the total SFR in a galaxy (equation 7). To test the effect of the ISRF intensity, we alter χ_{int} to be proportional to $\text{SFR} \times (r_{\text{s}}/r_{\text{SFR}})^2$ where $r_{\text{s}} = 3$ and 10 kpc. In these test models, the ISRF is stronger in a more compact galaxy for a given SFR. We find that this alteration only decreases L'_{CO} and M_{H_2} in low-mass galaxies, and that massive galaxies are little affected. We also note that the cosmic background radiation χ_{ext} is generally weaker than χ_{int} , and thus does not significantly impact our results.

The dust optical depth τ is another important parameter. In equation (9), the optical depth τ is proportional to an uncertain factor $f_{\text{dust}}/(as)$ that involves dust-to-metal fraction, grain size and density. Decreasing $f_{\text{dust}}/(as)$ can effectively lower L'_{CO} because of stronger ISFR. If we assume a lower $f_{\text{dust}}/(as)$ than the fiducial value, our CO-LF shown in Fig. 5 becomes inconsistent with the observations. In the extreme case of $\tau = \infty$, our results at $z = 0$ are still consistent with the observations within the error range (although see Section 5.2).

DESPOTIC can treat a different calculation mode by, for example, assuming a spherical cloud as radially stratified multiple shells with different optical depths. The multi-zone computation is thought to be more accurate than the single-zoned model we use in this study. Li et al. (2018) perform convergence tests using DESPOTIC and conclude that the eight-zoned model is sufficient to produce a converged result. We have repeated the same post-processing computations with the eight-zoned model, and have found that the results are essentially unchanged statistically from the fiducial case.

5.2 Evolution of ISM properties

The apparent discrepancy between our model and the ASPECS observations at high redshift (Section 4.2.1) may suggest evolution of ISM structure in galaxies. At $z \gtrsim 1.5$ –2, our model predicts lower $L'_{\text{CO}(1-0)}$ and higher M_{H_2} than the observational estimates. Compared with ASPECS, the luminosities of high- J lines $L'_{\text{CO}[J-(J-1)]}$ are systematically lower at high redshift. The trend of producing large H_2 masses appears to be opposite to the result of Popping et al. (2019), who find significantly lower M_{H_2} than the ASPECS at high redshift, although their model reproduces the H_2 mass at low-redshift observations. This may suggest ISM structure evolution over redshift.

We identify each galaxy as a gravitational bound object, whereas radio observations capture a galaxy’s CO emission within a beam size. This procedure may affect the total amount of $L'_{\text{CO}(1-0)}$ and M_{H_2} . Using the IllustrisTNG simulation, Popping et al. (2019) examine the systematic ‘aperture bias’. The resulting H_2 mass functions are not significantly different at high redshift between the two cases of using the SUBFIND grouping and the 3.5 arcsec aperture assuming the ASPECS observations.

We also find that assuming a large τ in our model does not signif-

icantly affect our CO-LFs and can only mildly reduce the difference. Even in the case of $\tau = \infty$, our model predicts lower L'_{CO} than the observations at high redshifts. The H_2 mass functions are hardly affected.

It has turned out that the cloud radius is the most important quantity that affects the CO line emission strengths. In Figs. 11 and 12, we plot CO-LFs with assuming ten times larger cloud radii as $r_{\text{cloud}} = 5\lambda_{\text{J}}$ (the magenta dashed lines). These test results are in better agreement with the ASPECS observations. However, $L'_{\text{CO}(1-0)}$ at $z = 0.5$ and 1.0 are larger than the observations of Orellana-González et al. (2020) if we adopt $r_{\text{cloud}} = 5\lambda_{\text{J}}$. Overall, we find that assuming enlarged r_{cloud} overpredicts the CO-LF at low redshift. Enlarging r_{cloud} hardly changes the H_2 mass functions. In determining λ_{J} (equation 4), our model does not take into account contributions by turbulent or magnetic pressure.⁹ Although the turbulent velocities in local galaxies are typically lower than the ISM sound velocity, it is known that star-forming galaxies at high redshift are highly turbulent with velocity dispersions of $\sim 100 \text{ km s}^{-1}$ (e.g. Förster Schreiber et al. 2009). Zhou et al. (2017) show illustrative comparison of velocity dispersions between star-forming galaxies observed at low and high redshifts. Ignoring the turbulent pressure can thus underestimate λ_{J} for high-redshift galaxies. Intriguingly, large turbulent velocities are thought to produce large, massive gas clouds (e.g. Dekel et al. 2009; Dessauges-Zavadsky et al. 2019). A possible prescription to match our results to the observations may be to introduce a fudge factor to increase r_{cloud} depending on redshift.

It may be possible that state-of-the-art cosmological hydrodynamics simulations are still unable to reproduce gas properties at high redshifts. The IllustrisTNG simulation reproduce a variety of statistical properties of observed galaxies such as stellar mass function, mass-metallicity relation and redshift-evolution of the cosmic SFR density (e.g. Vogelsberger et al. 2013; Genel et al. 2014; Nelson et al. 2018b; Naiman et al. 2018; Pillepich et al. 2018). However, it has not been fully examined whether the properties of the local ISM are compatible with real galaxies. Inoue & Yoshida (2019) have demonstrated that clumpiness of high-redshift disc galaxies can strongly depend on the ISM model (EOS of star-forming gas) assumed in simulations while global properties such as stellar and gas masses and SFRs are almost unchanged. Davé et al. (2020) analyse by post-processing various cosmological simulations with the same method to calculate $L'_{\text{CO}(1-0)}$ and M_{H_2} . They find that the results do not converge between different sets of simulations. Hayward et al. (2020) post-process the IllustrisTNG and original Illustris simulations to reproduce number counts of submillimetre galaxies (SMGs) at the redshift $z = 2$. They find that utilising IllustrisTNG significantly underpredicts the number of bright SMGs although their result using the original Illustris simulation is consistent with observations. They argue that this is because galaxies of IllustrisTNG have lower dust masses (metallicities) and SFRs than those of the original Illustris. Bright SMGs generally have quite high SFRs in observations, and this fact implies that such SMGs are expected molecular-rich. Our results predicting the low CO luminosities may stem from the same reason.

⁹ If the computation of λ_{J} includes the turbulent and magnetic pressure, γP_{CNM} in equation (4) is replaced with $\gamma P_{\text{CNM}} + \rho_{\text{CNM}}(v_{\text{turb}}^2 + v_{\text{A}}^2)$, where v_{turb} and v_{A} are turbulent and Alfvén velocities of the CNM (e.g. Federrath & Klessen 2012).

6 CONCLUSIONS AND SUMMARY

We utilise the IllustrisTNG simulation and populate unresolved gas clouds whose sizes are approximated as ‘thermal’ Jeans lengths of CNM. Adopting DESPOTIC, our method can compute not only CO(1-0) but also higher- J lines, calculate H_2 mass.

For galaxies at the redshift $z = 0$, we can reproduce the LF of CO(1-0) obtained by xCOLD GASS. Our values of α_{CO} are consistent with those estimated for the observed galaxies. Although we assume the simple model to approximate the radiation fields, the distribution of model α_{CO} is in agreement with the results of the more detailed model of Narayanan et al. (2012). We find that about ten per cent of H_2 in the Universe resides in galaxies with $M_{\text{star}} \lesssim 10^9 M_{\odot}$. These dwarfs have significantly low molecular abundances, which may be a reason for their low SF efficiencies.

For high-redshift galaxies, our method underpredicts CO luminosities. We find that we can mitigate the discrepancy of the CO-LFs if we enlarge the cloud sizes by a factor of ten, which corresponds to assuming a larger λ_J than the ‘thermal’ Jeans lengths in high-redshift galaxies. Highly turbulent states of galaxies observed in high-redshift Universe is expected to suppress gravitational collapse in small scales and lead to the formation of large and massive clouds. Thus, our results imply the redshift-evolution of ISM properties in molecular-rich and star-forming galaxies.

Our method enables direct comparison between simulations and observations. It forms the basis for a wealth of future studies, including mock observations using simulations and evaluation for potential biases in kinematic analyses using gas densities and velocity dispersion estimated from measurements of CO intensities and line widths.

ACKNOWLEDGEMENTS

This study was supported by World Premier International Research Center Initiative (WPI), NAOJ ALMA Scientific Research Grant Number 2019-11A, MEXT, Japan and by SPPEXA through JST CREST JPMHCR1414. SI receives the funding from KAKENHI Grant-in-Aid for Young Scientists (B), No. 17K17677, and HY receives the funding from Grant-in-Aid for Scientific Research (No. 17H04827 and 20H04724) from the Japan Society for the Promotion of Science (JSPS). The numerical computations presented in this paper were carried out on the analysis servers, the general-purpose PC cluster and Cray XC50 at Center for Computational Astrophysics, National Astronomical Observatory of Japan.

DATA AVAILABILITY

The data underlying this article will be shared on reasonable request to the corresponding author.

REFERENCES

Accurso G., et al., 2017, *MNRAS*, **470**, 4750
 Armillotta L., Krumholz M. R., Di Teodoro E. M., 2020, *MNRAS*, **493**, 5273
 Behroozi P. S., Wechsler R. H., Conroy C., 2013a, *ApJ*, **762**, L31
 Behroozi P. S., Wechsler R. H., Conroy C., 2013b, *ApJ*, **770**, 57
 Behroozi P., Wechsler R. H., Hearin A. P., Conroy C., 2019, *MNRAS*, **488**, 3143
 Bolatto A. D., Wolfire M., Leroy A. K., 2013, *ARA&A*, **51**, 207
 Catinella B., et al., 2018, *MNRAS*, **476**, 875
 Daddi E., et al., 2015, *A&A*, **577**, A46

Davé R., Crain R. A., Stevens A. R. H., Narayanan D., Saintonge A., Catinella B., Cortese L., 2020, arXiv e-prints, p. arXiv:2002.07226
 Decarli R., et al., 2016, *ApJ*, **833**, 69
 Decarli R., et al., 2019, *ApJ*, **882**, 138
 Dekel A., Sari R., Ceverino D., 2009, *ApJ*, **703**, 785
 Dessauges-Zavadsky M., et al., 2019, *Nature Astronomy*, **3**, 1115
 Diemer B., et al., 2019, *MNRAS*, **487**, 1529
 Draine B. T., 2011, *Physics of the Interstellar and Intergalactic Medium*. Princeton University Press
 Federrath C., 2018, *Physics Today*, **71**, 38
 Federrath C., Klessen R. S., 2012, *ApJ*, **761**, 156
 Fletcher T. J., Saintonge A., Soares P. S., Pontzen A., 2020, preprint (astro-ph/2002.04959), p. arXiv:2002.04959
 Förster Schreiber N. M., et al., 2009, *ApJ*, **706**, 1364
 Genel S., et al., 2014, *MNRAS*, **445**, 175
 Giovanelli R., et al., 2005, *AJ*, **130**, 2598
 Girichidis P., et al., 2020, *Space Sci. Rev.*, **216**, 68
 Glover S. C. O., Federrath C., Mac Low M. M., Klessen R. S., 2010, *MNRAS*, **404**, 2
 Gnedin N. Y., Kravtsov A. V., 2011, *ApJ*, **728**, 88
 Grassi T., Bovino S., Schleicher D. R. G., Prieto J., Seifried D., Simoncini E., Gianturco F. A., 2014, *MNRAS*, **439**, 2386
 Hayward C. C., et al., 2020, arXiv e-prints, p. arXiv:2007.01885
 Heyer M., Dame T. M., 2015, *ARA&A*, **53**, 583
 Inoue S., Yoshida N., 2019, *MNRAS*, **488**, 4400
 Jones M. G., Haynes M. P., Giovanelli R., Moorman C., 2018, *MNRAS*, **477**, 2
 Keating L. C., et al., 2020, arXiv e-prints, p. arXiv:2001.08197
 Krumholz M. R., 2014, *MNRAS*, **437**, 1662
 Krumholz M. R., 2017, *Star Formation*. World Scientific Publishing Co. Pte. Ltd., doi:10.1142/10091
 Kuhlen M., Krumholz M. R., Madau P., Smith B. D., Wise J., 2012, *ApJ*, **749**, 36
 Lagos C. D. P., Baugh C. M., Lacey C. G., Benson A. J., Kim H.-S., Power C., 2011, *MNRAS*, **418**, 1649
 Li Q., Narayanan D., Davé R., Krumholz M. R., 2018, *ApJ*, **869**, 73
 Li Y., Gu M. F., Yajima H., Zhu Q., Maji M., 2020, *MNRAS*, **494**, 1919
 Licquia T. C., Newman J. A., 2015, *ApJ*, **806**, 96
 Naiman J. P., et al., 2018, *MNRAS*, **477**, 1206
 Narayanan D., Krumholz M., Ostriker E. C., Hernquist L., 2011, *MNRAS*, **418**, 664
 Narayanan D., Krumholz M. R., Ostriker E. C., Hernquist L., 2012, *MNRAS*, **421**, 3127
 Nelson D., et al., 2018a, arXiv e-prints, p. arXiv:1812.05609
 Nelson D., et al., 2018b, *MNRAS*, **475**, 624
 Obreschkow D., Croton D., De Lucia G., Khochfar S., Rawlings S., 2009, *ApJ*, **698**, 1467
 Orellana-González G., et al., 2020, *MNRAS*, **495**, 1760
 Pakmor R., Marinacci F., Springel V., 2014, *ApJ*, **783**, L20
 Pillepich A., et al., 2018, *MNRAS*, **473**, 4077
 Popping G., Behroozi P. S., Peebles M. S., 2015, *MNRAS*, **449**, 477
 Popping G., et al., 2019, *ApJ*, **882**, 137
 Puchwein E., Haardt F., Haehnelt M. G., Madau P., 2019, *MNRAS*, **485**, 47
 Saintonge A., et al., 2017, *ApJS*, **233**, 22
 Schäbe A., Romano-Díaz E., Porciani C., Ludlow A. D., Tomassetti M., 2020, arXiv e-prints, p. arXiv:2003.04329
 Springel V., Hernquist L., 2003, *MNRAS*, **339**, 289
 Springel V., White S. D. M., Tormen G., Kauffmann G., 2001, *MNRAS*, **328**, 726
 Springel V., Di Matteo T., Hernquist L., 2005, *MNRAS*, **361**, 776
 Vallini L., Pallottini A., Ferrara A., Gallerani S., Sobacchi E., Behrens C., 2018, *MNRAS*, **473**, 271
 Vogelsberger M., Genel S., Sijacki D., Torrey P., Springel V., Hernquist L., 2013, *MNRAS*, **436**, 3031
 Weinberger R., et al., 2017, *MNRAS*, **465**, 3291
 Wolfire M. G., McKee C. F., Hollenbach D., Tielens A. G. G. M., 1995, *ApJ*, **453**, 673
 Yepes G., Kates R., Khokhlov A., Klypin A., 1997, *MNRAS*, **284**, 235

Zhou L., et al., 2017, [MNRAS](#), 470, 4573

This paper has been typeset from a \TeX/L\TeX file prepared by the author.